Active photonic wireless power transfer into live tissues

Juho Kim[a,b], Jimin Seo[a], Dongwuk Jung[a,b], Taeyeon Lee[a,b], Hunpyo Ju[a], Junkyu Han[a], Namyun Kim[a], Jinmo Jeong[a,b], Sungbum Cho[a,b], Jae Hun Seol[a], and Jongho Lee[a,b,1]

[a]School of Mechanical Engineering, Gwangju Institute of Science and Technology (GIST), 61005 Gwangju, Republic of Korea; and [b]Research Institute for Solar and Sustainable Energies, GIST, 61005 Gwangju, Republic of Korea

Recent advances in soft materials and mechanics activate development of many new types of electrical medical implants. Electronic implants that provide exceptional functions, however, usually require more electrical power, resulting in shorter period of usages although many approaches have been suggested to harvest electrical power in human bodies by resolving the issues related to power density, biocompatibility, tissue damage, and others. Here, we report an active photonic power transfer approach at the level of a full system to secure sustainable electrical power in human bodies. The active photonic power transfer system consists of a pair of the skin-attachable photon source patch and the photovoltaic device array integrated in a flexible medical implant. The skin-attachable patch actively emits photons that can penetrate through live tissues to be captured by the photovoltaic devices in a medical implant. The wireless power transfer system is very simple, e.g., active power transfer in direct current (DC) to DC without extra circuits, and can be used for implantable medical electronics regardless of weather, covering by clothes, in indoor or outdoor at day and night. We demonstrate feasibility of the approach by presenting thermal and mechanical compatibility with soft live tissues while generating enough electrical power in live bodies through in vivo animal experiments. We expect that the results enable long-term use of currently available implants in addition to accelerating emerging types of electrical implants that require higher power to provide diverse convenient diagnostic and therapeutic functions in human bodies.

photonic power transfer | biomedical implants | bioelectronics | flexible electronics

Biomedical electronic implants could help enhancing people's quality of life as well as lifespan through standalone diagnostics and treatments in human bodies (1–4). However, replacement surgeries are unavoidable when batteries integrated in the implants, usually taking more than half of the whole volume, are depleted (5). For long-term uses, diverse approaches have been developed to provide sustainable electrical power in human bodies (6–8) using electrochemical reactions (e.g., biofuel cells) (9–12) or mechanical movements of organs (e.g., breathing, heart-beating, muscles) (13–18) with aims of improving power density and reliability for practical uses (19–21). Inductive wireless power transfer by coupling radio-frequency electromagnetic fields is widely being used to charge rigid devices with cradles to take advantages of convenient alignment for higher transfer efficiency (21–28). For smaller devices, however, as the efficiency drops significantly and fine alignment over deformable biological tissues by patients can be challenging (22, 23), renovative methods (29, 30) should be considered.

Recent work by us and others introduces alternative approaches that demonstrate potential for providing reliable power with photovoltaics in bodies (31–34). However, implanted photovoltaics relying on ambient light may generate low power indoors, limit implantable exposed body regions to face or hands, and require long routing of electrical wires from the exposed regions (face or hands) to target organs. The difficulties may discourage their practical uses. Here, we

present a concept of the active photonic power transfer that overcomes the difficulties by actively transporting photon energy through potentially any regions of live bodies, covered or not by clothes, close to the target organs by introducing a full system of a skin-attachable light-source patch as a photon transmitter, and a photovoltaic array as a photon receiver integrated in a flexible medical implant in a live body. The reported system includes the thin, flexible, scalable, skin-attachable light source patch and enables sufficient wireless power transfer to relatively small and thin medical implants without concern about fine alignment over deformable tissues, limited ambient light intensity, limited implantable regions, or long routing wires in body for use in indoor or outdoor at day and night. The structural designs including bridges and direct integration of the micro-light emitting diodes (LEDs) onto metal heat sinks provide mechanical compatibility with the deformable live tissues and efficient thermal dissipation. In vivo demonstration of regulating heart rates of an animal model with the transferred power to the electronic implant proves feasibility of the concept.

Results and Discussion

Fig. 1A shows a conceptual illustration of the photonic wireless power transfer into a live body to sustainably operate a flexible medical electronic implant. The thin light-source patch attached on skin emits light consisting of photons whose energy and penetration depth depends on their wavelength. For example, a photon with a wavelength of 670 nm carries 1.85 eV and penetrates through live tissues about 2.5 mm (35), deeper than the dermis of human skin as illustrated in the blue dashed box of Fig. 1A. With photovoltaic (PV) devices integrated in a thin

---

flexible electronic implant, the photons can be captured and converted into electricity in the live body to sustainably power the medical electronic implant for diagnosis and therapy. Fig. 1B demonstrates the penetration of light through the live tissues. The glowing red light through the human fingers is visible even though a light source (4 × 4 LEDs) is completely covered by the fingers. More detailed measurements of optical transmittance through an isolated biological tissue (hairless mouse skin, SKH1-Hr[hr], thickness: ~0.55 mm) with an optical spectrometer (avaspec-ULS2048L, Avantes Corp.) and double-integrating spheres indicate relatively high transmittance (60–70%, optical window) at the higher wavelength (>600 nm) while relatively low transmittance of around 30–50% at 450–600 nm, as shown with the blue line in Fig. 1C. With the light-source materials whose peak electroluminescence (EL) spectrum (e.g., 670 nm, AlGaInP, red line in Fig. 1C) is within the optical window, a high portion (e.g., 60–70% for the mouse skin) of photons (photon energy: 1.85 eV) should be able to penetrate through the biological tissue and they can be absorbed and converted into electricity by the effect with the PV materials whose bandgap (e.g., GaAs, $E_g = 1.42$ eV) is lower than the photon energy (1.85 eV).

Fig. 1D shows a pair of the illuminating skin-attachable micro-LED light-source patch (AlGaInP, 670 nm, details in the later paragraphs) and the flexible PV device array (GaAs, $E_g = 1.42$ eV) placed under the isolated hairless mouse skin. The current–voltage characteristics of the PV device array under a standard AM1.5G and a red-light illumination with variable intensity are given in *SI Appendix*, Fig. S1. Fig. 1 *E* and *F* show the conceptual drawing and photograph of the micro-LED patch attached on a mouse. The patch generates photons (red light) into the body without any complicated driving circuits other than a conventional 3-V battery (CR2025). The skin-attached patch is advantageous as it can provide photons reliably from the skin surface even when the skin is covered by cloth at lower ambient light as shown in Fig. 1G.

The transmitter (light-source patch) should be close to the receiver (PV devices) as much as possible, i.e., the light-source patch should be attachable to the skin to maximize power transfer as the light intensity is inversely proportional to the distance squared. However, attaching a light-source patch on deformable skin should involve designs to minimize mechanical or thermal damages to the devices themselves or biological tissues. Fig. 2 *A* and *B* show the exploded and integrated view of the design to maximize mechanical flexibility and thermal dissipation while maintaining the density of the micro-LEDs. The key design factors of the light source patch include the bridges for relieving mechanical strain in the flexible metal interconnects, and heat sinks not only for efficient thermal dissipation but also for direct electrical contact with the micro LEDs, realized
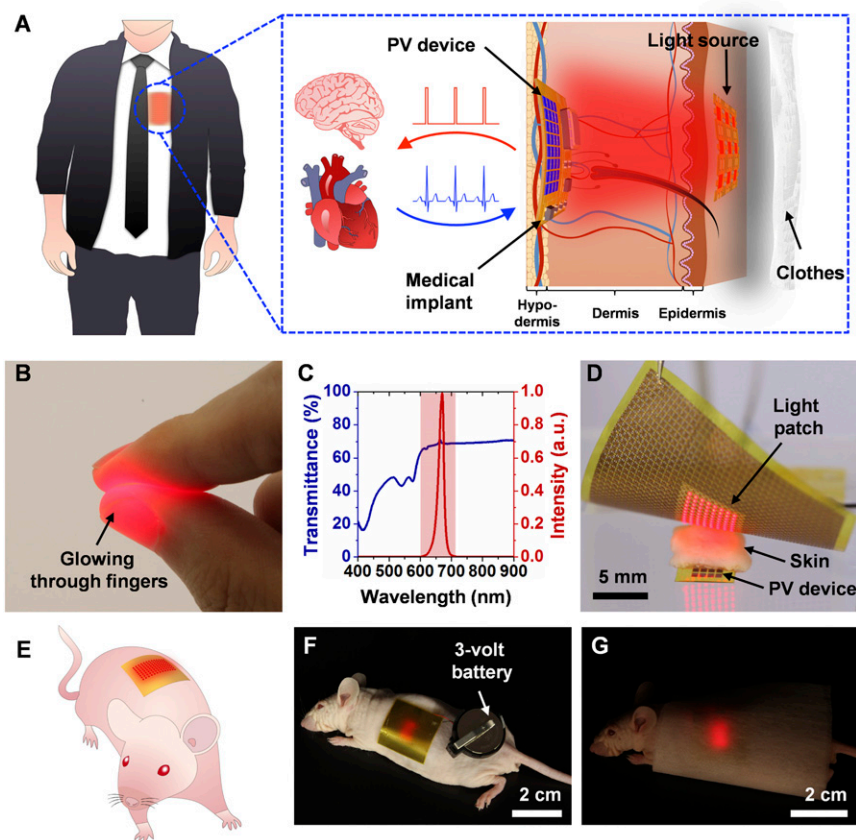
Fig. 1. Photonic wireless power transfer with the skin-attachable light-source patch. (*A*) Conceptual illustration of the photonic wireless power transfer into a live body to operate a medical implant sustainably in the body. The light source attached on skin illuminates light that is reachable onto the receiver (PV devices) that is integrated in the flexible medical implant. (*B*) Image of fingers glowing due to the transmitted light through the live tissue even though a light source is completely covered by the fingers. (*C*) Optical transmittance (blue line) through an isolated hairless mouse skin (thickness: ~0.55 mm, SKH1-Hr[hr]) and EL spectrum (red line) of a red micro-LED. Both of them were measured by an optical spectrometer (avaspec-ULS2048L, Avantes Corp.). The EL spectrum (~670 nm) of the micro-LED is over the wavelength (>650 nm) on which the transmittance is relatively high (~70%). (*D*) A photo of the skin-attachable micro-LED light-source patch illuminating over an isolated hairless mouse skin under which PV devices are placed. (*E*) Conceptual drawing and (*F*) photograph of the micro-LED light-source patch attached on the back of a mouse. A conventional 3-V battery (CR2025) is enough to turn on the skin-attachable micro-LED light-source patch without any complicated circuits. (*G*) Glowing micro-LED patch attached on the mouse skin under the cloth.
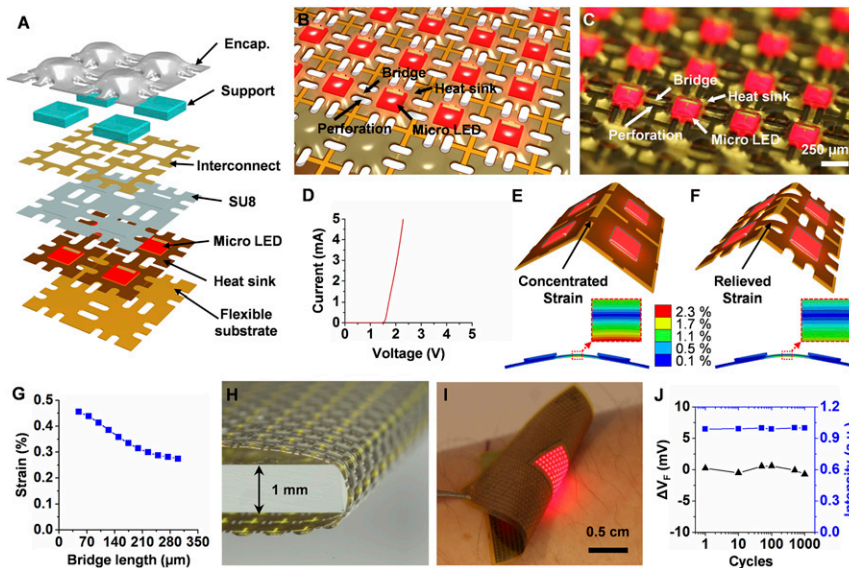
Kim et al.

www.manaraa.com

Fig. 2. Designs and properties of the light-source patch. (*A* and *B*) Exploded and integrated view of the skin-attachable micro-LED light-source patch. The key design includes the bridges for relieved strain and heat sinks not only for efficient thermal dissipation but also for direct electrical contact. (*C*) Optical image of the fabricated light-source patch with the AlGaInP micro-LEDs (8 × 13, each size: 250 × 250 μm², thickness: ~4.1 μm) turned on. (*D*) Current–voltage characteristic of the fabricated micro-LED. (*E*) Illustration and FEA without the bridge design; mechanical strain is concentrated in the interconnects. (*F*) Illustration and FEA with the bridge design; the interconnect is more relaxed, i.e., higher bending radius in the interconnect. For the same bending of the patches (radius: 1.5 mm), FEA indicates that the maximum strain in the metal interconnect with and without the bridge is 0.285 and 0.455%, respectively. (*G*) FEA results of the maximum strain in the metal interconnect depending on bridge length (50–300 μm). (*H*) Photograph of the skin-attachable light-source patch wrapped over a glass slide (thickness: 1 mm). (*I*) Photograph of the patch under bending while detaching from skin. (*J*) Measurements of the forward voltage difference (ΔV$_F$, black triangles) at the current of 50 mA and optical intensity (blue rectangles) of the patch over mechanical cycles (bending radius of ~3 mm, up to 1,000) of bending and unbending. No noticeable performance degradation is shown during the tests.

through cold-welding (pressure: ~1.4 MPa, temperature: 95 °C, more details in *Materials and Methods* and *SI Appendix*) the thin micro-LEDs directly onto the heat sinks. The perforations around the bridges are also beneficial in sweat evaporation when the patch is attached to skin. The cross-sectional and lateral designs are given in *SI Appendix*, Figs. S6 and S7, respectively. Fig. 2*C* shows an optical image of the complete light-source patch with the illuminating micro-LEDs (AlGaInP, 8 × 13, each: 250 × 250 μm², thickness: ~4.1 μm) designed and fabricated from an epitaxially grown AlGaInP wafer. The current–voltage of the micro LED is given in Fig. 2*D*. The forward-bias is around 1.73 V at 1 mA. More details of the fabrication process are in *Materials and Methods* and *SI Appendix*.

Without the bridge design, mechanical strain is concentrated in the metal interconnect because the regions covered by the thick heat sink (5 μm) are more rigid as illustrated in Fig. 2*E*. However, with the bridge design for the same density of the LEDs, the interconnect is more relaxed, i.e., less strain in the interconnect, as in Fig. 2*F*. For the same bending radius of 1.5 mm, finite element analysis (FEA) indicates that the maximum strain in the metal interconnects with and without the bridge design is 0.285 and 0.455%, respectively. Fig. 2*G* shows FEA results of the maximum strain in the metal interconnect as a function of the bridge length (50–300 μm). The results clearly indicate that the longer bridge relieves the maximum strain in the metal interconnect better. The results also agree well with the relative strains predicted from the simple geometric model presented in *SI Appendix*, Fig. S7. The fabricated light-source patch is flexible enough to be wrapped over a glass slide (thickness: 1 mm) as in Fig. 2*H* or to be bent while detaching from skin as in Fig. 2*I*. The thin sticky encapsulation (Silbione RT Gel 4717 A/B; Bluestar Silicone) provides adhesion to the skin. Repetitive bending (radius: ~3 mm) and unbending cycles

did not show degradation in the electrical performances such as the forward voltage difference (ΔV$_F$ at 50 mA, black triangles) and optical intensity (blue rectangles) of the patch.

Incorporating heat sinks and direct integration of the micro-LEDs on the heat sinks enables more efficient thermal dissipation. The experimental and computational analysis of thermal properties of the micro-LED patches (LEDs: 5 × 5, patch size: 1 × 1 cm²) fabricated with and without heat sinks appears in Fig. 3. Without a heat sink (Fig. 3*A*), the micro-LEDs are integrated onto a flexible polyimide (PI) film as shown with the optical image in Fig. 3*B*. As the thermal conductivities of the surrounding materials are relatively low (SU-8: 0.2 W/m·K, PI: 0.12 W/m·K), the measurement with a thermal infrared (IR) imager (fotric-228, FOTRIC) indicates that the maximum surface temperature rise of the freestanding micro-LED patch is 87.2 °C with an injection current of 30 mA as shown in Fig. 3*C*. The measurement result (87.2 °C) is comparable with the FEA result (88.7 °C, COMSOL Multiphysics) in Fig. 3*D*. In contrast, direct cold welding of the micro-LEDs onto the metal heat sink as illustrated in Fig. 3*E* dissipates generated heat more efficiently as the heat sink (Au/Ni/Ti/Cu = 150 nm/10 nm/200 nm/5 μm) has much higher thermal conductivity (401 W/m·K). The fabricated patch with the heat sink appears in Fig. 3*F*. For the same current injection (30 mA), the measurement (Fig. 3*G*) clearly reveals that the surface temperature rise (28 °C) of the patch with the heat sink is much lower than the patch without a heat sink (87.2 °C). The FE analysis indicates that the surface temperature rise goes down to 24.3 °C with the heat sink. A natural convection boundary (convection heat transfer coefficient: 25 W/m²·K) (36) is assumed on the top and bottom surface in the FEA. The parameters used in the FEA and the current–voltage characteristics of the fabricated LED are given in *SI Appendix*, Figs. S10 and S11, respectively.

Characterization of the thermal or optical properties depending on the various heat sinks provides design guidance of the skin-attachable flexible power transfer patches. Fig. 3*I* shows the measurements of the surface temperature rise (ΔT) of the freestanding patches with the various heat sink designs with respect to the applied electrical power. The heat sink designs (no heat sink: red square; narrow and thin: violet circle; wide and thin: green diamond; wide and thick: blue triangle) are given in *SI Appendix*, Fig. S12. With the "wide and thick" heat sink, the temperature rise is the lowest (28 °C at 57.9 mW). Degradation of the optical properties such as intensity (Fig. 3*J*) and full width at half-maximum (Fig. 3*K*, FWHM defined in *SI Appendix*, Fig. S13) of the patch is the smallest (i.e., high optical intensity and low bandwidth broadening) with the wide and thick heat sink as the patch dissipates generated heat more efficiently. The intensity and FWHM were measured with the patches fixed on a polydimethylsiloxane (PDMS)-coated glass slide when measuring with an optical spectrometer. The temperature rise of the attached patch on skin (Fig. 3*L*, blue diamond, ΔT = 6.7 °C at 58.2 mW, wide and thick) is much lower than that of the

freestanding patch in air (red diamond, ΔT = 35.8 °C at 56.2 mW) because of conduction through the biological tissue. The surface temperature (41.2 °C, ΔT = 6.7 °C) of the patch is lower than the standard minimum surface temperature (44 °C for 6 h) at which thermal contact burn can occur (37) (ASTM C1055-03).

The photonic power transfer performance can be affected by skin thickness or lateral alignment between the light source (LED) and receiver (PV). For the performance measurements only, without consideration of thermal or mechanical characteristics, we prepared various LED arrays (horizontal pitch: 2.1 mm and vertical pitch: 1.425 mm for 4 × 4 array, pitch: 1.3 mm for 4 × 1, 6 × 1, 8 × 1, 10 × 1 arrays) with commercially available devices (SML-P12UT, Rohm Semiconductor). Fig. 4*A* shows the custom experimental setup with which we can adjust vertical distance and lateral alignment between the LED array (4 × 4) fixed on the two-axis tilting holder on top and PV device (700 × 560 μm^2, thickness: ~4 μm) mounted on the microstage at the bottom. Details are in *Materials and Methods*. Measurement results of the normalized current transferred from the LED array to the PV device through different thickness of mouse skins
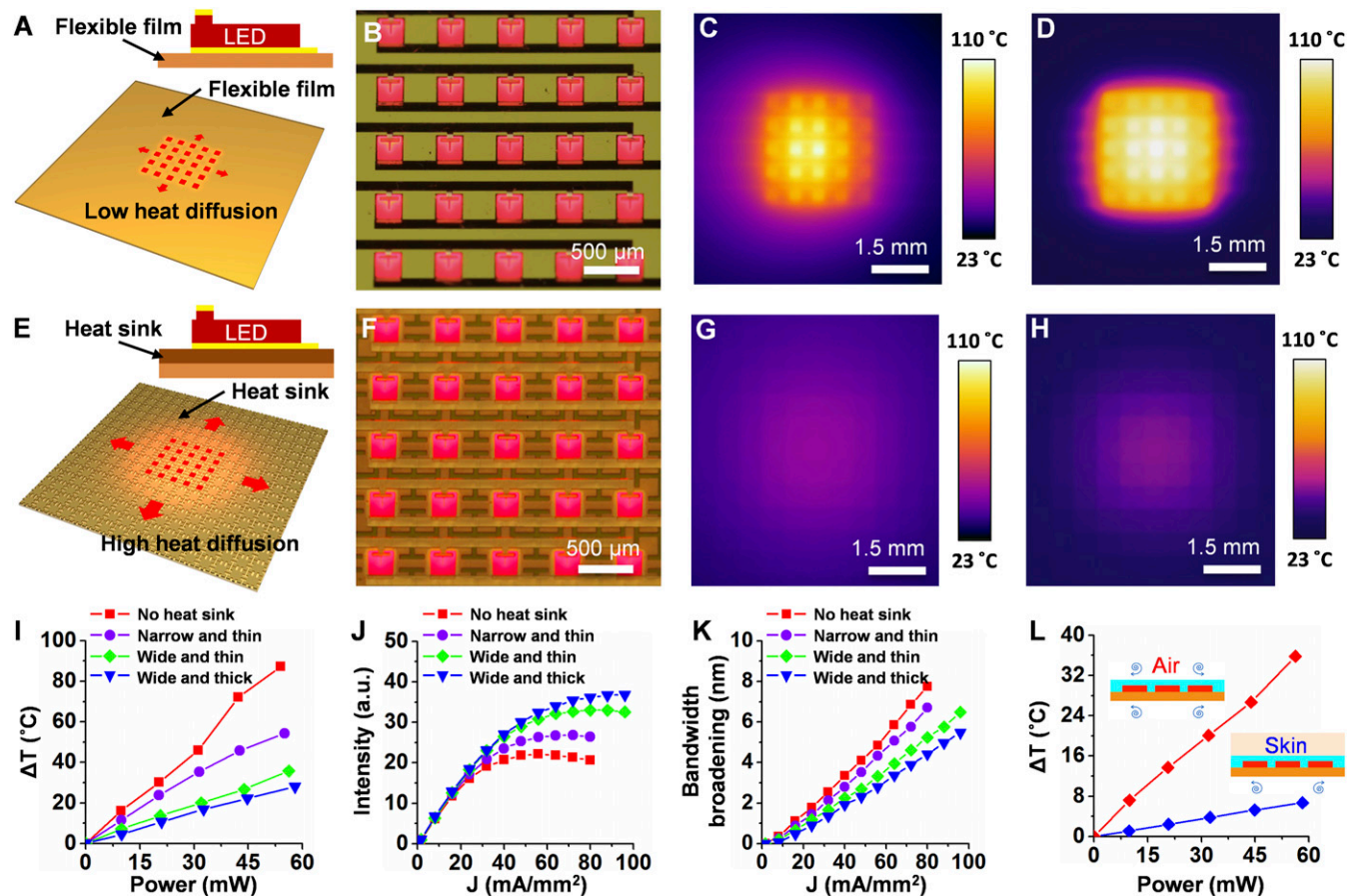

Fig. 3. Thermal characteristics. (*A*) Schematic illustrations of the micro-LEDs integrated onto a flexible film (PI) without a metal heat sink. The upper illustration is the cross-sectional view. (*B*) Optical microscope image of the fabricated micro-LEDs patch (LEDs: 5 × 5, patch size: 1 × 1 cm^2) without a heat sink, and (*C*) corresponding thermal IR image (fotric-228, FOTRIC) and (*D*) FEA result (COMSOL Multiphysics) of the freestanding patch in air with an input current of 30 mA. (*E*) Schematic illustrations of the micro-LEDs in direct contact with a metal heat sink. (*F*) Optical image of the micro-LEDs cold-welded directly onto the metal heat sink (Au/Ni/Ti/Cu = 150 nm/10 nm/200 nm/5 μm), and (*G*) corresponding thermal IR image and (*H*) FEA result of the freestanding patch with the same input current 30 mA. The FEA and experimental results clearly indicate that the heat sink significantly lowers the surface temperature. (max temperature rise: 88.7 °C → 24.3 °C by FEA and 87.2 °C → 28 °C by measurements) (*I*) Measurement results of the surface temperature rise (ΔT) of the freestanding light-source patches with various heat sink designs (red square: no heat sink; violet circle: narrow and thin; green diamond: wide and thin; blue triangle: wide and thick as illustrated in *SI Appendix*, Fig. S12) depending on the applied electrical powers. Measurements of (*J*) optical intensity and (*K*) FWHM of the patches fixed on a PDMS-coated glass slide. (*L*) Measurements of the surface temperature rise of the attached wide and thin patch on human skin (blue diamond) and the freestanding patch in air (red diamond).
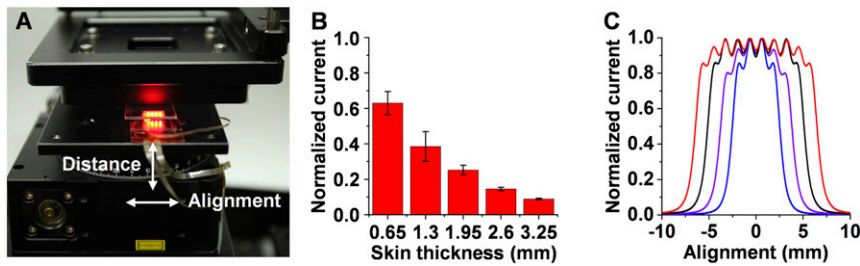
Fig. 4. Performance characteristics depending on skin thickness and alignment. (*A*) Experimental setup for the measurements. (*B*) Normalized current transferred through mouse skins in different thickness. Layers of mouse skin (1 layer: 0.65 mm) are stacked for thicker ones. (*C*) Normalized current depending on lateral alignment between the LED array and PV device. LED arrays (pitch: ~1.3 mm): 4 × 1 (blue), 6 × 1 (violet), 8 × 1 (black), 10 × 1 (red).

appear in Fig. 4*B*. We used multiple layers of isolated mouse skin (1 layer: ~0.65 mm) for thicker penetration depth. As expected, the wirelessly transferred current is inversely proportional to the skin thickness as more attenuation occurs due to higher probability of absorption in thicker skin tissues.

The transferred current is relatively less sensitive to lateral alignment between the light source and receiver as shown in Fig. 4*C*. There is about 10% variation in the transferred current depending on the alignment with the LED array (pitch: ~1.3 mm). The results also indicate that the covered region (>90% in transferred current) robust to the misalignment can be expanded by simply increasing the array size (number of LEDs), e.g., covered region: ~2.0 mm for 4 × 1, ~4.3 mm for 6 × 1, ~7.4 mm for 8 × 1, ~9.7 mm for 10 × 1 array. The property could be beneficial for wireless power transfer through deformable tissues without fine alignment.

In vivo experiments with live mouse models demonstrate feasibility of the concept of photonic wireless power transfer into bodies. The tiny implantable stimulator (size: 1 × 0.65 cm^2) custom-designed and fabricated on a flexible film (PI, 12.5 μm) appears in Fig. 5*A*. Instead of a large battery whose volume is usually more than 50% of a conventional pacemaker (estimated volume: 10–15 cm^3), the stimulator includes the very thin PV devices (blue box, 4 × 8, GaAs, each: 700 × 560 μm^2, each active area: 0.35 mm^2, total active area: 11.1 mm^2, thickness: ~4 μm) and small rechargeable microbattery (purple box, size: 3.2 × 2.5 mm^2, thickness: 0.9 mm, Seiko) in addition to the low-dropout voltage regulator (green box) and pulse generator (red box) consisting of inverters, resistors, and capacitors. The average current and power consumption of the stimulator are ~1.9 μA and ~2.3 μW, respectively. Details of the fabrication and circuit diagram are in *Materials and Methods* and *SI Appendix* (*SI Appendix*, Fig. S14). The stimulator is fully implanted through a small incision (Fig. 5*B*) other than the wires for performance characterization only as shown in *SI Appendix*, Fig. S15.

Attaching (upper image in Fig. 5*C*) followed by turning on (~110 mW, lower image) the light-source patch enables photonic wireless power transfer to the implanted stimulator as shown with the *in vivo* current–voltage (red line) and power–voltage (blue line) characteristics in Fig. 5*D*. The wirelessly transmitted power to the implanted stimulator (active PV area: 0.11 cm^2) is 8.2 μW (at 2.12 V) which is higher than the required power consumption of the custom-built stimulator (~2.3 μW) or commercially available pacemakers (1–10 μW). The wirelessly transmitted power (~8.2 μW) through the skin is enough to generate the periodic stimulating pulses (Fig. 5*E*, frequency: ~3.2 Hz, pulse width: 0.9 ms, duty cycle: 0.29%) and charge the extra power (~5.9 μW) to the built-in microbattery as shown with the charge–discharge characteristics in Fig. 5*F*. The measurements were conducted with the implanted stimulator that is wirelessly powered by the skin-attachable patch alone. Even after

the light-source patch is turned off at 106 min, the implanted stimulator powered by the charged battery continues to operate for extra 90 min.

A thoracotomy (Fig. 5*G*) was conducted to demonstrate heart-rate regulation of the mouse with the implanted stimulator while being wirelessly powered by the skin-attached patch. The implanted stimulator generates pulses with a frequency of 3.3 Hz (red line in Fig. 5*H*). As soon as the output lead wires from the implanted stimulator is brought in contact with the right atrium and left ventricle of the mouse in bradycardia (0–5.5 s, blue line in Fig. 5*H*) at 5.5 s, the heart starts to beat regularly at ~3.3 Hz, the same frequency of the generated pulses from the implanted stimulator.

The *in vivo* experiments successfully demonstrate a key biomedical function (electrical stimulation) of most fully implantable medical electronics such as cardiac pacemakers, deep brain stimulators (DBS), spinal cord stimulators, and many others. The transferred *in vivo* power (~8.2 μW, ~74.1 μW/cm^2 for the active PV area) with the full system is already around the power consumption for commercial stimulators (e.g., cardiac pacemakers: 1–10 μW) depending on operating modes. For a cardiac pacemaker requiring 10 μW, the minimum active PV area is 13.5 mm^2. It should be noted that foreign-body reaction may cause extra tissues (such as fibroblasts and immune cells) to grow over the implant (38). The tissue may further scatter or absorb the transmitted light, lowering electrical power transfer performance. When designing the photonic power transfer system, the effects by the extra tissues should be carefully considered. With industry-standard optoelectronic devices, the power can be further raised to a level of 100 μW. Details are in *SI Appendix*, Fig. S16. Although the similar amount of power may be achievable by other approaches such as inductive coupling, the photonic power transfer provides a combination of clear benefits: 1) very simple circuits (power transfer from DC to DC), 2) no requirement of fine alignment over deformable tissues, 3) simple scaling up or down the power by adjusting device size.

Conclusions

In conclusion, the design, fabrication, and *in vivo* experiments with the platforms at the level of a full system prove feasibility of the active wireless photonic power transfer for medical electronic implants. The *in vivo* demonstration includes the key biomedical function. The designs prove that potential issues such as mechanical and thermal compatibility can be relieved and controlled. The transferred power by the approach even with the custom-fabricated optoelectronic devices is already enough to charge and operate the implantable stimulator, and should be improved much higher with an industry standard fabrication in dedicated facilities with optimized epistructures, leading to accelerating developments of medical implants with advanced and

Kim et al.

www.manaraa.com

diverse functions that are limited by a limited electrical power in live bodies.

Materials and Methods

Preparation of the AlGaInP Micro-LEDs on a GaAs Wafer. The AlGaInP micro-LEDs (~4.1 μm) were prepared on a GaAs wafer with an epitaxially grown LED structure as shown in *SI Appendix*, Fig. S3. Depositing and lifting-off process of the thin metals (20-nm Ti/60-nm Au) formed the top metal electrodes on the p-GaAs top contact layer. Wet etching with a mixture of citric acid ($C_6H_8O_7$, monohydrate, J.T. Baker Inc.) and hydrogen peroxide (H_2O_2, 35%, OCI Company Ltd.) defined the top contact regions. The active device areas (250×250 μm^2) were defined by a photoresist (AZ5214E, 1.8 μm, AZ Electronic Materials) masking and a sequential wet chemical etching process with hydrochloric acid (HCl, 35%, OCI Company Ltd.) and phosphoric acid (H_3PO_4, 85%, H_2O_2, 35%, OCI Company Ltd.). A protecting photoresist (PR) layer (AZ9260, ~23 μm, Microchem) covering the defined devices was formed by coating with the PR and baking at 110 °C for 15 m, followed by a rehydration for 1 h, ultraviolet (UV) exposure (2,200 mJ/cm^2), and development (~17 m).

Direct Integration of the Micro-LEDs onto the Metal Heat Sink Layer. We prepared a film stamp by patterning etch holes ($r = 150$ μm) on a PI ~25-μm film and coating a thin PDMS ~10-μm layer on the PI film. After contacting the film stamp to the PR-coated micro-LEDs on the GaAs wafer, we applied heat (10 m, 104 °C) and pressure (40 g weight) to improve an adhesion between the stamp and LEDs by slightly melting and resolidifying the PR layer. After releasing the LEDs by removing the sacrificial layer, we deposited the bottom electrode (Ni 10 nm/Au 150 nm) with an electron beam evaporator, followed by bringing the bottom electrode in direct contact

with a metal heat sink layer [Au/Ni/Ti/Cu = 150 nm/10 nm/200 nm/(2 or 5 μm)] deposited on a flexible substrate (PI, ~12.5 μm). Applying heat (95 °C, 10 m) and pressure (~1.4 MPa) established a direct bonding of the micro-LEDs onto the metal heat sink layer. The metal heat sink layer also serves as a bottom electrical interconnect between LEDs. Cleaning with acetone removed the photoresist without detaching the bonded micro-LEDs from the metal heat sink layer. More details are given in *SI Appendix*, Fig. S4.

Forming the Interconnections and Encapsulations. As the heat sink layer serves as bottom electrical interconnects, the layer was patterned by a masked wet chemical etching with a mixture of HCl, H_2O_2, and H_2O. For top electrical interconnection, we sputtered metal films (Ni 100 nm/Au 200 nm) and defined the interconnection lines by a lifting-off process after forming via-holes to top electrodes of the micro-LEDs through a thin spin-casted epoxy insulation layer (SU-8, ~2 μm, Microchem). The bridges and perforations were formed with a dry etching process with a reactive ion etcher. We spin-casted and cured UV-curable resin (NOA 61, 270 μm × 270 μm × 20 μm, Norland Products) as a mechanical support for the micro-LEDs. Finally, we screen-printed the sticky encapsulation layer (Silbione RT Gel 4717 A/B; Bluestar Silicone) to prevent the perforations from being filled up. Curing the sticky encapsulation layer completes the fabrication process. More details with schematic illustrations are given in *SI Appendix*, Figs. S5 and S6.

Preparation of the Implantable Stimulator. Fabrication of the implantable stimulator starts with directly integrating PV devices (4 × 8, 4 in series and 8 in parallel, GaAs, each: 700 × 560-μm^2, thickness: ~4 μm) onto a flexible PI film (thickness: 12.5 μm) in the similar way of integrating the micro-LEDs. After spin-casting a thin epoxy insulation layer (SU-8, ~2 μm, Microchem) and forming via-holes over the electrodes, we deposited and lifted off the metal
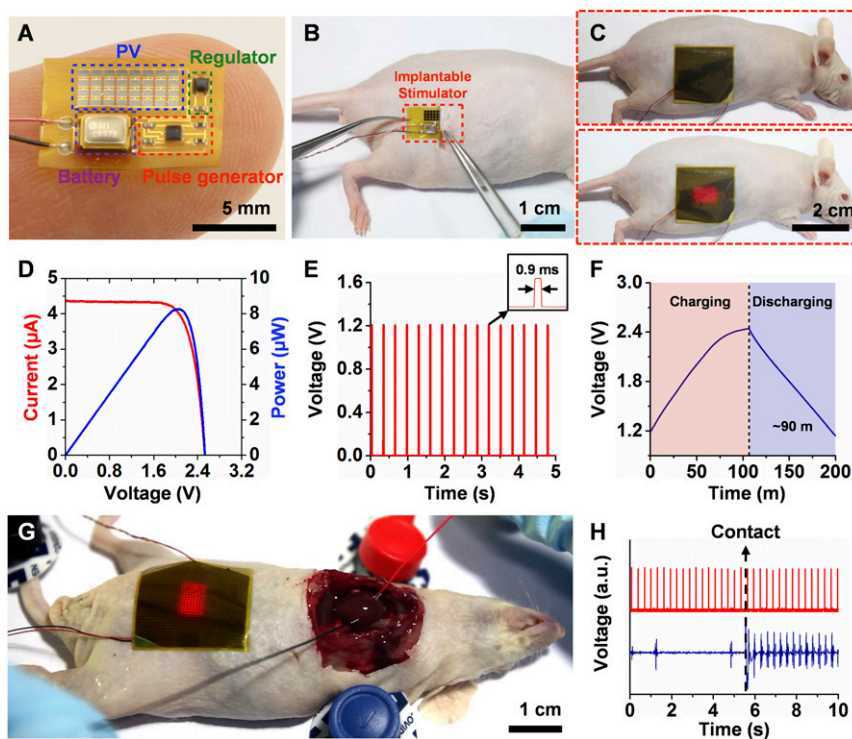

Fig. 5. Demonstration of photonic wireless power transfer to an implanted medical stimulator. (*A*) Optical image of the implantable stimulator (size: 1 × 0.65 cm^2) integrated on a flexible PI film with PV devices (blue box, 4 × 8, GaAs, each: 700 × 560 μm^2, thickness: ~4 μm), a low-dropout voltage regulator (green box), a rechargeable microbattery (purple box, Seiko), and a pulse generator (red box). (*B*) The stimulator is fully implanted other than the wires used for performance measurements only. (*C*) Photographs of the light-source patch attached on the mouse skin. (*D*) In vivo current–voltage (red line) and power–voltage (blue line) characteristics of the power wirelessly transferred to the implanted stimulator from the attached light-source patch. (*E*) Periodic stimulating pulses (frequency: ~3.2 Hz, pulse width: 0.9 ms, duty cycle: 0.29%) measured from the implanted stimulator. (*F*) Charge–discharge characteristics of the implanted stimulator powered wirelessly by the skin-attachable patch. The wirelessly transferred power (~8.2 μW) is enough to operate the stimulator (~2.3 μW) and charge the extra power (~5.9 μW) to the microbattery. (*G*) In vivo demonstration of stimulating the mouse heart with the implanted stimulator while being wirelessly powered by the skin-attachable patch. (*H*) Generated pulses (~3.3 Hz, red line, *Upper*) from the implanted stimulator, and measured electrocardiogram signals (blue line, *Lower*) of the mouse in bradycardia. The lead wires from the implanted stimulator are brought into contact with the heart at 5.5 s.

Kim et al.

www.manaraa.com

layers (Ti 60 nm/Au 300 nm) to interconnect the PV devices. The metal deposition process also formed the pads for the pulse generator, low-dropout voltage regulator, and rechargeable microbattery (CPX3225A752D, 3.2 × 2.5 mm², thickness: 0.9 mm, Seiko Instruments), which were integrated on the pads with aid of a biocompatible conductive adhesive (H20E, Epoxy Technology). Finally, we encapsulated the implantable stimulator with a PDMS layer after forming norland optical adhesive (NOA 61, Norland Products) supports for the ICs and the PV devices.

Measurements of Electrical Properties. The current–voltage characteristics of the PV devices and the micro-LEDs were measured with a source measure unit (B2902A, Keysight Technologies). We characterized the performance of the PV devices with and without covering by the isolated mouse skin (thickness: ∼0.55 mm) under illumination of a solar simulator (LCS-100, Oriel Instruments) and a commercial red LED (sunplus 2835, ∼650 nm, Lumileds). When characterizing the performance of the micro-LEDs, we used a pulsed sweep mode including off time (period: 200 ms, pulse width: 10 ms, duty cycle: 5%) between measurement points instead of a DC sweep mode to avoid a temperature rise from previous measurements.

Measurements of Optical Properties. We measured the transmittance of the isolated mouse skin (thickness: ∼0.55 mm, SKH1-Hr^{hr}) with an optical spectrometer (avaspec-ULS2048L, Avantes Corp.) by collecting scattered light with double-integrating spheres. We also characterized the intensity and EL spectrum of the micro-LED patches (5 × 5, "No heat sink," "Narrow and thin," "Wide and thin," Wide and thick) with the optical spectrometer for each injected current density.

Measurements of Thermal Properties. We measured the thermal properties of the freestanding micro-LED patches (5 × 5, No heat sink, Narrow and thin, Wide and thin, Wide and thick) with a noncontacting thermal IR camera (fotric-228, FOTRIC) after waiting to stabilize the temperature for 1 min for each injected current. The emissivity of the thermal camera was set to 0.95 for the surface of the micro-LED patches encapsulated with a layer of PDMS (39). Then, the injected current was converted to the operating power to quantify the temperature rise as a function of the operating power that is more directly related to the generated heat. For temperature measurements of the micro-LED patch (5 × 5, wide and thin) attached on human skin, we placed a thermocouple between the patch and human skin and measured the temperature with the thermometer (HH147U, OMEGA Engineering Inc.) after waiting for 7 min to stabilize the temperature.

Performance Measurements Depending on Skin Thickness and Alignment. We measured transferred current depending on skin thickness and alignment with the custom apparatus that includes a two-axis tilting stage on top and a three-dimensional translation microstage at the bottom. The two-axis tilting stage enables parallel alignment of the top holder and the bottom microstage. We attached the LED array on the top holder and mounted the PV device on the stage. For measurements depending on skin thickness, we measured transferred current from the PV device placed under a layer of isolated mouse skin at a constant distance (∼2 mm) with an operating current (20 mA) to the LED array (4 × 4). We adjusted the distance between the light source and receiver as much as average thickness (∼0.65 mm) when we added another layer of isolated skin. For measurements depending on lateral alignment, we measured transferred current with the LED arrays (pitch: ∼1.3 mm, 4 × 1, 6 × 1, 8 × 1, 10 × 1, operating current: 5 mA) fixed on top by adjusting the position of the PV device mounted on the custom motorized microstage (resolution: 0.1 μm)

Animal Experiments. We conducted the animal experiments by following the guidelines of Gwangju Institute of Science and Technology (GIST) Institutional Animal Care and Use Committee (GIST-2019-077) approval. Hairless mice (SKH1-Hrhr) were anesthetized by intraperitoneal injection of anesthetics (0.3 mL, ketamin 50, ∼50 mg/kg, rompun, ∼5 mg/kg, Yuhan). We inserted the implantable stimulator through an incision on the skin sterilized with a povidone iodine (povidone, Firson). For *in vivo* measurements, we closed the incision with two stitches but with the electrical wires connected to the implanted stimulator for the purpose of performance measurements only. We measured the current–voltage and charge–discharge characteristics of the implanted stimulator under the irradiation of the attached micro-LED light-source patch (injection current: 60 mA) on the skin. We also conducted a thoracotomy to demonstrate the functionality of the stimulator powered by the skin-attachable light-source patch.

Data Availability. All data are present in the main text, *SI Appendix*, and Movies S1 and S2.

1. D. A. Nathan, S. Center, C. Y. Wu, W. Keller, An implantable synchronous pacemaker for the long term correction of complete heart block. *Am. J. Cardiol.* **11**, 362–367 (1963).
2. K. Bazaka, M. Jacob, Implantable devices: Issues and challenges. *Electronics (Basel)* **2**, 1–34 (2012).
3. H. Cagnan, T. Denison, C. McIntyre, P. Brown, Emerging technologies for improved deep brain stimulation. *Nat. Biotechnol.* **37**, 1024–1033 (2019).
4. Y. Yu, H. Y. Y. Nyein, W. Gao, A. Javey, Flexible electrochemical bioelectronics: The rise of in situ bioanalysis. *Adv. Mater.* **32**, 1902083 (2020).
5. G. T. Hwang, M. Byun, C. K. Jeong, K. J. Lee, Flexible piezoelectric thin-film energy harvesters and nanosensors for biomedical applications. *Adv. Healthc. Mater.* **4**, 646–658 (2015).
6. E. Gibney, The inside story on wearable electronics. *Nature* **528**, 26–28 (2015).
7. C. Dagdeviren, Z. Li, Z. L. Wang, Energy harvesting from the animal/human body for self-powered electronics. *Annu. Rev. Biomed. Eng.* **19**, 85–108 (2017).
8. A. Ben Amar, A. B. Kouki, H. Cao, Power approaches for implantable medical devices. *Sensors* **15**, 28889–28914 (2015).
9. A. Zebda et al., Mediatorless high-power glucose biofuel cells based on compressed carbon nanotube-enzyme electrodes. *Nat. Commun.* **2**, 370 (2011).
10. L. Halámková et al., Implanted biofuel cell operating in a living snail. *J. Am. Chem. Soc.* **134**, 5040–5043 (2012).
11. E. Katz, K. MacVittie, Implanted biofuel cells operating in vivo–Methods, applications and perspectives–Feature article. *Energy Environ. Sci.* **6**, 2791 (2013).
12. A. Zebda et al., Single glucose biofuel cells implanted in rats power electronic devices. *Sci. Rep.* **3**, 1516 (2013).
13. Q. Zheng et al., In vivo powering of pacemaker by breathing-driven implanted triboelectric nanogenerator. *Adv. Mater.* **26**, 5851–5856 (2014).
14. C. Dagdeviren et al., Conformal piezoelectric energy harvesting and storage from motions of the heart, lung, and diaphragm. *Proc. Natl. Acad. Sci. U.S.A.* **111**, 1927–1932 (2014).
15. A. Zurbuchen et al., Endocardial energy harvesting by electromagnetic induction. *IEEE Trans. Biomed. Eng.* **65**, 424–430 (2018).
16. G.-T. Hwang et al., Self-powered deep brain stimulation via a flexible PIMNT energy harvester. *Energy Environ. Sci.* **8**, 2677–2684 (2015).
17. Z. Li, G. Zhu, R. Yang, A. C. Wang, Z. L. Wang, Muscle-driven in vivo nanogenerator. *Adv. Mater.* **22**, 2534–2537 (2010).
18. M. Han et al., Three-dimensional piezoelectric polymer microsystems for vibrational energy harvesting, robotic interfaces and biomedical implants. *Nat. Electron.* **2**, 26–35 (2019).
19. S. Cosnier, A. Le Goff, M. Holzinger, Towards glucose biofuel cells implanted in human body for powering artificial organs: Review. *Electrochem. Commun.* **38**, 19–23 (2014).
20. H. Basaeri, D. B. Christensen, S. Roundy, A review of acoustic power transfer for biomedical implants. *Smart Mater. Struct.* **25**, 123001 (2016).
21. A. Kim, M. Ochoa, R. Rahimi, B. Ziaie, New and emerging energy sources for implantable wireless microdevices. *IEEE Access* **3**, 89–98 (2015).
22. A. P. Chandrakasan, N. Verma, D. C. Daly, Ultralow-power electronics for biomedical applications. *Annu. Rev. Biomed. Eng.* **10**, 247–274 (2008).
23. X. Lu, P. Wang, D. Niyato, D. I. Kim, Z. Han, Wireless charging technologies: Fundamentals, standards, and network applications. *IEEE Comm. Surv. and Tutor.* **18**, 1413–1452 (2016).
24. B. Ziaie, M. D. Nardin, A. R. Coghlan, K. Najafi, A single-channel implantable microstimulator for functional neuromuscular stimulation. *IEEE Trans. Biomed. Eng.* **44**, 909–920 (1997).
25. M. Catrysse, B. Hermans, R. Puers, An inductive power system with integrated bidirectional data-transmission. *Sens. Actuators A Phys.* **115**, 221–229 (2004).
26. B. Lenaerts, R. Puers, An inductive power link for a wireless endoscope. *Biosens. Bioelectron.* **22**, 1390–1395 (2007).
27. M. Ghovanloo, K. Najafi, A wireless implantable multichannel microstimulating system-on-a-chip with modular architecture. *IEEE Trans. Neural Syst. Rehabil. Eng.* **15**, 449–457 (2007).

www.manaraa.com

28. P. Li, R. Bashirullah, A wireless power interface for rechargeable battery operated medical implants. *IEEE Trans. Circuits Syst., II Express Briefs* **54**, 912–916 (2007).

29. J. S. Ho *et al.*, Wireless power transfer to deep-tissue microimplants. *Proc. Natl. Acad. Sci. U.S.A.* **111**, 7974–7979 (2014).

30. D. R. Agrawal *et al.*, Conformal phased surfaces for wireless powering of bioelectronic microdevices. *Nat. Biomed. Eng.* **1**, 43 (2017).

31. K. Song *et al.*, Subdermal flexible solar cell arrays for powering medical electronic implants. *Adv. Healthc. Mater.* **5**, 1572–1580 (2016).

32. E. Moon, D. Blaauw, J. D. Phillips, Subcutaneous photovoltaic infrared energy harvesting for bio-implantable devices. *IEEE Trans. Electron Dev.* **64**, 2432–2437 (2017).

33. L. Lu *et al.*, Biodegradable monocrystalline silicon photovoltaic microcells as power supplies for transient biomedical implants. *Adv. Energy Mater.* **8**, 1703035 (2018).

34. L. Bereuter *et al.*, Energy harvesting by subcutaneous solar cells: A long-term study on achievable energy output. *Ann. Biomed. Eng.* **45**, 1172–1180 (2017).

35. J. Wang *et al.*, Opportunities and challenges of fluorescent carbon dots in translational optical imaging. *Curr. Pharm. Des.* **21**, 5401–5416 (2015).

36. F. P. Incropera, D. P. DeWitt, T. L. Bergman, A. S. Lavine, *Fundamentals of Heat and Mass Transfer*, (John Wiley & Sons, ed. 6, 2007).

37. ASTM International, *ASTM C1055-99 - Standard Guide for Heated System Surface Conditions That Produce Contact Burn Injuries*, (ASTM International, West Conshohocken, PA, 1999).

38. J. M. Morais, F. Papadimitrakopoulos, D. J. Burgess, Biomaterials/tissue interactions: Possible solutions to overcome foreign body response. *AAPS J.* **12**, 188–196 (2010).

39. B. H. Ha *et al.*, Acoustothermal heating of polydimethylsiloxane microfluidic system. *Sci. Rep.* **5**, 11851 (2015).

ENGINEERING

Kim et al.

www.manaraa.com